




Chiral polymer-induced hydroxyapatite for promoting bone regeneration

Zongying Zhang^{a,b,1}, Bing Liang^{a,1}, Dan Wang^{a,b}, Ying Zhang^a, Zhongmin Geng^{a,*} , Dongming Xing^{a,c,**}

^a Cancer Institute, The Affiliated Hospital of Qingdao University, Qingdao University, Qingdao, 266071, China

^b School of Basic Medicine Qingdao University, Qingdao University, Qingdao, 266071, China

^c School of Life Sciences, Tsinghua University, Beijing, 100084, China

ARTICLE INFO

Keywords:

Chiral
Poly(levorotatory-hydroxyapatite)
Vascular remodeling
Bone regeneration

ABSTRACT

Chirality is one of the basic characteristics of living matter, yet the effect of chiral polymers on osteogenesis is seldom studied. Thus, it is necessary to deeply recognize the behaviors of chiral polymers in osteogenic processes, which can be beneficial for the development of bone repair materials. In this work, chiral hydroxyapatite (HAP) was constructed simply using poly(levorotatory/dextral-tartaric acid) as the guest of the chiral transfer system. We studied the influence of chiral HAPs on the migration and differentiation of pre-osteoblasts, and angiogenesis of endothelial cell in vitro. The results showed that poly(levorotatory-tartaric acid)-induced HAP did promote vascular remodeling and exhibited excellent impact on osteogenetic differentiation by improving the related gene and protein expression, whereas no significant change was observed in poly(dextral-tartaric acid) or poly(racemic-tartaric acid) induced HAP, respectively. This study highlighted the effects of chiral polymers on osteogenic potential, which laid the groundwork for the development of biomaterials for bone regeneration.

1. Introduction

Chirality was the critical biochemical feature of living beings, which had a significant influence the constituting a complex feature of organs and tissue [1]. The human body comprised a large number of biological molecules with specific handedness, such as proteins, nucleic acids, tissues and cells [2–6]. Therefore, a deep study of the effect of chirality would provide valuable insights and guidance to generate advanced biomaterials. Previous studies had demonstrated that small chiral molecules accelerate angiogenesis and osteogenesis in the process of bone regeneration [7], yet the effect of chiral oligomers/polymers was rarely investigated, and little was known about the biological mechanisms.

Hydroxyapatite (HAP) had been considered to be one of the

important substitute materials for bone repair and regeneration due to its inherent advantages including great biocompatibility, crystal controllability, and stability [8–10]. Recently, Shuai et al. found that the biopolymer scaffold blended with graphene oxide-HAP and biopolymer poly-L-lactic acid could improve environment on cell proliferation and adhesion [11]. Moussa et al. used chiral tartaric acid to induce selective nucleation and crystallization of calcium phosphate and enhanced the mechanical properties of calcium phosphate bioceramics [12]. The formation of calcium phosphate crystal included three dynamic steps, 101, 001 and 201. The addition of D-TAR kept the crystal growing stably, however, the addition of L-TAR interacted with the 101 step and limited the crystal size [12]. During the formation of natural bone tissue, different hierarchical chiral structures were only related to collagen

Abbreviations: HAP, Hydroxyapatite; HAPs, Hydroxyapatites; TAR, Tartaric acid; PTAR, Ploytartaric acid; D-TAR, Dextral-tartaric acid; L-TAR, Levorotatory-tartaric acid; Rac-TAR, Racemic-tartaric acid; PDTA, Poly(dextral-tartaric acid); PLTA, Poly(levorotatory-tartaric acid); PRTA, Poly(racemic-tartaric acid); PD-HAP, Poly(dextral-hydroxyapatite); PL-HAP, Poly(levorotatory-hydroxyapatite); PRac-HAP, Poly(racemic-hydroxyapatite); FT-IR, Fourier transform infrared spectroscopy; XRD, X-ray diffraction; XPS, X-ray photoelectron spectrometer; UV–vis, Ultraviolet–visible light; CD, Circular dichroism; SEM, Scanning Electron Microscopy; TEM, Transmission electron microscope; SAED, Selected area electron diffraction; P/S, Penicillin plus streptomycin; CCK-8, Cell Counting Kit-8; ALP, Alkaline phosphatase; ARS, Alizarin Red S; PBS, Phosphate-buffered saline; RT-qPCR, Real-Time Quantitative Reverse Transcription-Polymerase Chain; VEGFA, Vascular endothelial growth factor A; Runx2, Runt-related transcription factor 2; Bglap, Bone gamma-carboxyglutamate (gla) protein; Sp7, Sp7 transcription factor; Col1a1, Collagen I α 1; BMP-2, Bone Morphogenetic Protein type 2; Jun, Jun proto-oncogene; AC, Adenylatecyclase.

* Corresponding author.

** Corresponding author. Cancer Institute, The Affiliated Hospital of Qingdao University, Qingdao University, Qingdao, 266071, China.

E-mail addresses: gzmin-qdu@qdu.edu.cn (Z. Geng), xdm_tsinghua@163.com (D. Xing).

¹ These authors contributed equally to this work.

<https://doi.org/10.1016/j.mtbio.2025.101460>

Received 6 October 2024; Received in revised form 26 December 2024; Accepted 3 January 2025

Available online 4 January 2025

2590-0064/© 2025 Published by Elsevier Ltd. This is an open access article under the CC BY-NC-ND license (<http://creativecommons.org/licenses/by-nc-nd/4.0/>).

peptide assembly at each level of bone structure [13–15]. In addition, Zhou et al. used chiral tartaric acid to induce the synthesis of chiral mesostructured hydroxyapatite film (CMHAPF), which had been demonstrated to be enantioselective to cells. They found that L-CMHAPF could promote adipose-derived mesenchymal stem cells (Ad-MSCs) adhesion and accelerate bone-marrow-derived mesenchymal stem cells osteogenic differentiation, while D-CMHAPF facilitated Ad-MSCs adipogenesis [16]. Moreover, the chiral structure also had an effect on angiogenesis, levorotatory calcium silicate hydrate films had been shown to promote bone healing by affecting angiogenesis [17]. Natural chiral oligomers/polymers (such as polysaccharides, peptides, and nucleic acids) can be used as chiral templates to induce the non-optically active species to form chiral structures by non-covalent bond interactions between guest and host [18,19]. However, the acquisition and storage of natural chiral polymers were undoubtedly difficult. It had been reported that artificially synthesized polymers can help to induce the nucleation and growth of HAP crystals [11,20]. Herein, chiral ploytartaric acid (PTAR) was employed as a guest in the chiral transfer system to induce chirality of the subject HAP. HAP was usually synthesized by hydrothermal synthesis, wet chemistry, combustion synthesis, and sol-gel synthesis, and the crystal formation process needed to be completed by high temperature sintering [21]. In this work, chiral HAPs were prepared by the chemical deposition method in the whole process at room temperature, and the pH was controlled to be alkaline, and the addition of chiral polytartaric acid improved its crystallinity, and then their physical and chemical characterizations were investigated. The effect of chiral HAPs on the migration and differentiation of pre-osteoblasts, endothelial cell migration, and angiogenesis were studied in vitro. The results revealed that chiral HAPs induced by poly(levorotatory-tartaric acid) (PLTA) efficiently promoted cell migration, angiogenesis, and osteogenic differentiation, whereas lower effect was observed in poly(dextral-tartaric acid) (PDTA) or poly(racemic-tartaric acid) (PRTA) induced HAP, respectively. This enantioselectivity was interpreted as the stereo matching between cells and chiral structures of HAP. This study provided evidence for exploring the biological differences caused by natural chiral substances in living organisms in bone regeneration.

2. Materials and methods

2.1. Chiral HAPs preparation

Based on previous reports [12,16,21], we used chemical precipitation to synthesize HAP, and added polyorganic acids to change the chirality of HAP during its formation. However we used different synthetic processes, this was different from what was previously reported. Heating dextral-tartaric acid (D-TAR), levorotatory-tartaric acid (L-TAR), and racemic-tartaric acid (Rac-TAR) at 160 °C or 120 °C for 1 h formed poly(dextral-tartaric acid) (PDTA), poly(levorotatory-tartaric acid) (PLTA), and poly(racemic-tartaric acid) (PRTA) [22]. Preparation of chiral HAPs: 1.2 M (NH₄)₂HPO₄ and 2 M CaCl₂ were respectively dissolved in 10 mL ddH₂O. 0.5 M or 0.8 M and polytartaric acid (PTAR) dissolved in 5 mL ddH₂O. Under conditions of rapid stirring, (NH₄)₂HPO₄ solution and PTAR solution were added drop by drop to the CaCl₂ solution. Finally, NH₃ • H₂O was added to the reaction system to regulate pH 10, and continued to stir for 1 h. Whereafter, the reaction products were deposited at room temperature for 48 h. Poly(dextral-hydroxyapatite) (PD-HAP), poly(levorotatory-hydroxyapatite) (PL-HAP), and poly(racemic-hydroxyapatite) (PRac-HAP) were obtained. The deposited products were flushed multiple times with ethanol and ddH₂O. These products were dried in a 65 °C oven. Before the biological experiment, the chiral HAPs were sterilized by soaking in 75 % ethanol for 24 h, and after the ethanol volatilized, they were sterilized by ultraviolet light for 48 h.

2.2. Scanning electron microscopy (SEM) study, transmission electron microscope (TEM) and select electron diffraction analysis (SEAD)

The different chiral HAPs were attached to the conductive adhesive and treated with gold for observation. A transmission electron microscope with resolution of 0.8 nm and operating voltage of 200 KV was used to photograph chiral HAPs, and selected electron diffraction analysis was performed.

2.3. Particle size analysis

Chiral HAPs were dispersed in aqueous solution and the size of chiral HAPs were measured using the Malvern Zetasizer Nano ZSE.

2.4. Fourier transform infrared spectroscopy (FT-IR), X-ray diffraction (XRD)

HAP powder solid as for Fourier infrared spectrometer, measuring the sample under the infrared transmittance. XRD patterns were recorded on an X-ray diffractometer at a rate of 10° min⁻¹, ranging from 5° to 80°.

2.5. X-ray photoelectron spectrometer (XPS) analysis

When the prepared samples were placed on the sample table and the vacuum degree of the instrument reached the required vacuum degree, the samples were measured. Origin 2021 was used for peak fitting.

2.6. Ultraviolet–visible light (UV–vis) analysis and circular dichroism (CD) analysis

Chiral HAPs were dispersed in water in a special colorimetric dish and measured using the UV–vis spectrometer and the circular dichroism spectrometer.

2.7. MC3T3-E1, L929, HUVEC cell culture

Before cell culture, the cell room and biosafety cabinet were disinfected with ultraviolet light. The frozen MC3T3-E1 cells and HUVEC cells were resuscitated in a 37 °C constant temperature water bath in advance. DMEM complete medium (89 % DMEM, 10 % FBS, 1 % P/S) was added to the cell-culture dish and the cell suspension was added for cell culture. When the cell number reached 80%–90 % in the culture dish, and the pancreatic enzyme was added for cell digestion at 37 °C. The digested cells were transferred to the centrifuge tube and added the medium for centrifugation, and the cell precipitation was re-suspended with the medium. The cell suspension was transferred to a new culture dish for culture. L929 cell was cultured using RPMI1640 (Meilun) complete medium (89 % RPMI1640, 10 % FBS, 1 % P/S). The culture method was the same as that of MC3T3-E1 cells and HUVEC cells.

2.8. Cell Counting Kit-8 (CCK-8) assay

The cells were co-cultured with chiral HAPs at different concentrations (50, 100, 200, 400 µg/mL), and the viabilities of the cells were detected. The cell medium was sucked away at a predetermined time, supplemented with a 10 % CCK-8 (Meilun) enhancement solution, and incubated in a cell incubator. After incubation for 1–4 h, the absorbance at 450 nm was measured with an enzyme label. Cell viability is calculated as follows:

Cell viability (%) = $\frac{As-Ab}{Ac-Ab} \times 100\%$ where As is the absorbance of the experimental hole (containing cells treated with chiral HAPs), Ac is the absorbance of the control hole (containing cells that have not been treated with chiral HAPs), Ab is the absorbance of blank hole (no cells, no chiral HAPs).

2.9. Cell live/dead staining

The cells were co-cultured with different groups of chiral HAPs and stained at a predetermined time. The Calcein-AM/PI double staining kit (Meilun) was used to prepare the dye working solution. The working solution was added to the cell pore plate, and cleaned with phosphate-buffered saline (PBS) (Meilun) at 37 °C for 15 min. The alive and dead cells were observed under a fluorescence microscope.

2.10. Actin cytoskeleton staining

Firstly, the medium mixture of different chiral HAPs was configured, and the sample concentration was selected to be 50 µg/mL. MC3T3-E1 cells were inoculated in 24-well plates and cultured with DMEM complete medium containing HAP. MC3T3-E1 cells were cultured for 3 days and stained. The cell medium was sucked away, the cells were cleaned with sterile PBS, and fixed with 4 % paraformaldehyde (Solarbio) for 30 min. 0.05 % Triton X-100 treated for 10 min, Actin-Tracker Red-555 (1:200) (Beyotime) diluted with PBS containing 5 % BSA was added to the cells and incubated at 37 °C away from light for 30 min. After dyeing, wash with PBS containing 0.05 % Triton X-100 3 times for 5 min each time. After drying, sealing the sheets with DAPI Fluoromount-G™ Anti-fluorescent quenched sealants (Yeasten). Then the laser confocal microscope was used to observe.

2.11. Scratch wound-healing assay

The cells were cultured with chiral HAPs at 400 µg/mL concentration in advance, digested and inoculated into the six-well plate, and scratched on the cell surface when the cells were overgrown. The difference in migration of different groups of cells to the scratched area was observed at the predetermined time. The scratch boundaries was the dividing line between the edge of the scratch and the unscratched area of the cell when the scratch is initially created. Quantification of blank scratch areas using ImageJ software. The closed area proved the ability of cells to migrate to the blank area. The closed area (%) = the blank area of the experimental group/the blank area of the control group × 100 %.

2.12. Cell migration experiment

The cells were pre-treated with 400 µg/mL chiral HAPs medium suspension. After the cells were overgrown, they were digested and re-suspended in a serum-free base medium for cell counting, so that the 200 µL cell suspension contained 2×10^4 cells. Preparing the Transwell chamber, adding 500 µL complete medium to the lower chamber and 200 µL pre-treated cell suspension to the upper chamber. The cells were cultured in a 37 °C incubator and their transfer abilities were measured at a predetermined time. The Transwell chamber was removed, cleaned with PBS, and then fixed with 4 % paraformaldehyde for 15 min. Then stained with 0.1 % crystal violet solution (Beyotime) for 15 min, cleaned with PBS, and the cells in the upper compartment were wiped away. The cells below the chamber were observed under an ordinary light microscope.

2.13. Angiogenesis experiment

HUVEC cells were co-cultured with different groups of chiral HAPs in advance and digested after cell overgrowth. Adding extracellular matrix (ECM) gel (Sigma) to the bottom of the chamber slide and place in the incubator until the ECM gel was set. The cells were then inoculated in groups, with 2×10^4 cells added to different wells. The tubule formation of HUVEC cells was observed by microscope after 6 h of normal culture. In this experiment, the number of branches points referred to the number of branches that new blood vessels send out from the main vessel trunk, which was an important indicator of the degree of

angiogenesis. More branches points usually mean more angiogenesis.

2.14. Alizarin Red S and alkaline phosphatase staining

MC3T3-E1 was co-cultured with three groups of chiral HAPs in 24-well plates, and cell fixation and staining were performed at a predetermined time. After culture for the appropriate time, the metabolic waste on the cell surface was carefully cleaned with PBS and fixed with 4 % paraformaldehyde. The fixed cells were washed three times with PBS. The cells were stained with 0.2 % Alizarin Red S (ARS) (Solarbio) dye solution (pH 8.3) and observed by microscope. The BCIP/NBT working solution (Beyotime) was prepared by diluting 10 µL of BCIP solution and 20 µL of NBT solution with 3 mL of alkaline phosphatase developing buffer. The BCIP/NBT working solution was added to the fixed cells and stained at 37 °C. After dyeing, wash three times with ddH₂O, dry the water, and take photos for observation.

2.15. Immunofluorescence staining of osteoblast protein

The primary antibodies used in this experiment were: Runx2 antibody (Affinity), ALP antibody (Affinity), and osteocalcin antibody (Affinity). After co-culture with chiral HAPs, the cells were fixed with 4 % paraformaldehyde. The cells were treated with 0.5 % TritonX-100 and then closed with 3 % BSA. After closure, the primary antibodies diluted with 3 % BSA solution were added and incubated at room temperature for 3 h. After incubation, wash with PBST (0.05 % Tween-20, 99.95 % PBS) 3 times for 10 min each time. Continuing incubation of an Alexa-Fluor 594 conjugated goat anti-rabbit IgG (H + L) Ab for 1 h at room temperature in a dark place. And washing with PBST 3 times for 10 min each time. The sheets were sealed with DAPI Fluoromount-G™ Anti-fluorescent quenched sealants. They were then transferred to laser confocal microscopy for observation.

2.16. Real-time quantitative reverse transcription-polymerase chain (RT-qPCR)

In the same way as above, MC3T3-E1 cells and HUVEC cells were co-cultured with different groups of chiral HAPs of 50 µg/mL in advance, and collected cells at a predetermined time. a. Total RNA Extraction. The cells were cleaned with PBS, RNA-easy (Vazyme) was added to cover the cell surface, and then blown down with a pipette and transferred to a centrifuge tube. Adding two-fifths of the volume of the RNase-free ddH₂O (Meilun) to the lysate, mix upside down, and let stand at room temperature for 5 min. Centrifuging at 12000 ×g for 15 min, absorbing the supernatant, adding an equal volume of isopropyl alcohol, mixing upside down, and leaving for 15 min. Centrifuging at 12000 ×g for 10 min, leaving white precipitate, washing three times with 75 % ethanol, and let dry. Dissolving in the right amount of RNase-free ddH₂O and measuring the concentration of RNA. b. Reverse Transcription. Taking 5 µg of RNA and adding it to the inversion system (TransGen), incubating at 25 °C for 10 min, 45 °C for 15 min, and finally 85 °C for 5 s. c. qPCR. 10 ng cDNA was taken as the template, 10 µL 2× Universal SYBR Green Fast qPCR Mix (ABclonal), 0.4 µL forward primer (10 µM) and 0.4 µL reverse primer (10 µM) (Tables S1 and S2), and supplemented with ddH₂O to 20 µL to serve as the qPCR reaction system. Then the qPCR reaction program was set up. With β-actin as the housekeeping gene, the relative expression of related genes was detected by the $2^{-\Delta\Delta Ct}$ method.

2.17. Statistical analysis

In this paper, particle size analysis, FT-IR, XRD, XPS and UV-vis and CD maps were all drawn using Origin 2021. All the statistical bar charts in this paper were completed using GraphPad 8.0. For the cell viability analysis, the scratch healing analysis, the cell migration assay, the tubule formation assay, the ALP/ARS staining analysis, the

immunofluorescence analysis, and the RT-qPCR assay, the data were expressed as the mean \pm standard error of the mean and were analyzed using the one-way ANOVA. However, the CCK-8 analysis used two-way ANOVA. The P -value < 0.05 was considered statistically significant. * $p < 0.05$, ** $p < 0.01$, *** $p < 0.001$, and **** $p < 0.0001$, ns: no difference.

3. Results and discussion

3.1. Characterization of chiral hydroxyapatite

In order to explore the characteristics of chiral HAPs, we first carried on the physical and chemical characterization of detection. PTAR, polymerized by TAR monomers under the heating condition (Fig. 1A), were used as guests of the chiral transfer system to induce the different nucleation and growth of HAP crystals [12,23]. First, the polymerization of PTAR was verified by FT-IR spectra, where the $\nu(\text{O-H})$ stretching vibrational peak of TAR obtained at 160 °C decreased significantly,

compared to that of TAR polymerized at 120 °C. The $-\text{C}=\text{O}$ stretching band of TAR was shown at 1712 cm^{-1} , while it appeared at 1730 cm^{-1} after high-temperature heating. The stretching intensity decreased with the temperature increasing. And the spectrum of the PTAR formed at 160 °C showed a weak band of an unprotonated carboxyl group at 1628 cm^{-1} (Fig. 1B). These demonstrated that the TAR molecules had been successfully dehydrated to form PTAR under heating.

The crystal structures of HAPs were induced by adding different chiral PTAR at room temperature (Fig. 1C). SEM was used to confirm the obtained structure of PTAR-induced HAPs (Fig. 1D). The crystal structures of chiral HAPs were hexagonal and relatively stable in size. As reflected from the DLS results shown in Fig. 1E, the average size of PD-HAP ($d = 2587\text{ nm}$) was larger than those of PL-HAP ($d = 1639\text{ nm}$) group and PRac-HAP ($d = 778.6\text{ nm}$) group (Fig. 1D). The structures of chiral HAPs were further verified by FT-IR. As shown in Fig. 1F, the $\nu(\text{O-H})$ bond appeared at $3500\text{--}2500\text{ cm}^{-1}$ and the $-\text{C}=\text{O}$ stretching band appeared at 1580 cm^{-1} in the PTAR-induced HAPs map. Meanwhile, this

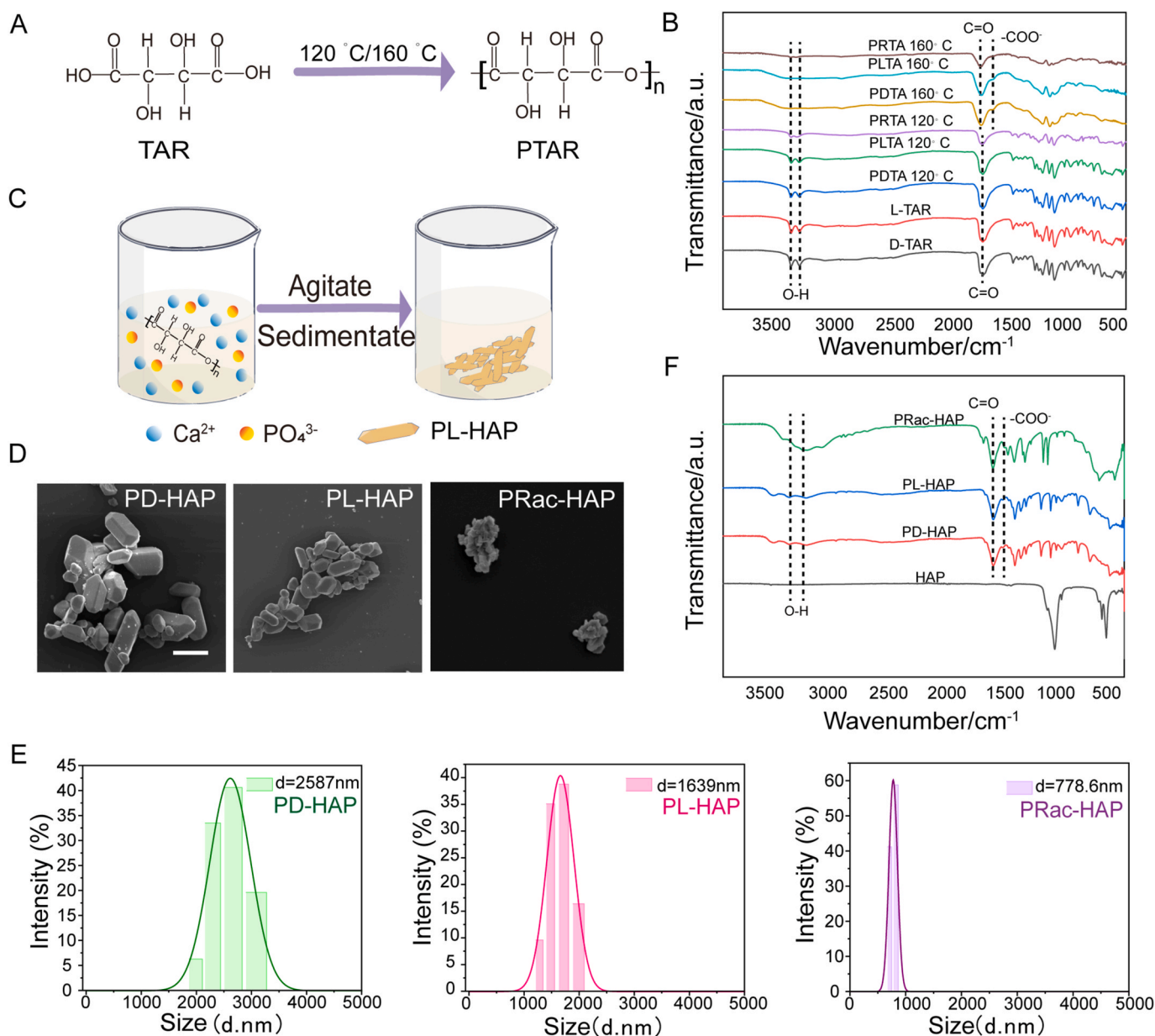


Fig. 1. The characteristics of the chiral HAPs. (A) Synthesis of PTAR. (B) FT-IR spectra of PD-HAP, PL-HAP and PRac-HAP. (C) Synthesis of the chiral HAPs, taking PL-HAP as examples. (D) SEM images of PD-HAP, PL-HAP and PRac-HAP. Scale bars: 2 μm. (E) Particle size distribution charts of PD-HAP, PL-HAP and PRac-HAP. (F) FT-IR spectra of PTAR.

also proved that the $\nu(\text{O-H})$ bond was weakened by dehydration during the formation of PTAR, and the peak of $-\text{COO}^-$ appeared at 1485 cm^{-1} , which affects the functional groups of chiral HAPs. Furthermore, the concentration of chiral PTAR inducers had little effect on HAP's important functional groups (Fig. S1). The peak intensity of the $\nu(\text{O-H})$ bond of chiral HAPs decreased with the increase of the treatment temperature of the PTAR, and the dehydration was strongly reactive at higher temperatures (Fig. S2).

The crystal structures of chiral HAPs were observed by TEM, and the morphologies of HAPs crystals were similar (Fig. 2A). In order to further investigate the crystallographic structure, the specific crystal structures were determined by SAED (Fig. 2B). It can be observed that the PD-HAP crystal had (002), (302) and (322) crystal faces, and the PL-HAP crystal had (110), (202) and (130) crystal faces, and PRac-HAP crystal had (002), (302) and (140) crystal faces, which were consistent with the crystal faces of the standard HAP crystal (JCPDS: 00-009-0432). A wide Angle XRD was further used to investigate the crystal structures of HAPs.

As shown in Fig. 2C, PD-HAP, PL-HAP and PRac-HAP all had characteristic crystal faces (110), (210) and (130) of standard HAP, which indicated that the crystallographic structure of HAP were not affected by the chiral polymers. The XPS images exhibited that the three HAPs contained C, O, Ca and P peaks (Fig. 2D–F). In order to explore the interaction between PTAR and HAP, the peak fitting of C1s was carried out, and it was found that the C element of PTAR was bonded with the hydroxyl group of HAP. UV–visible spectroscopic analyses showed that the absorption peaks of chiral HAPs were at 253 nm when two different concentrations of PTAR were added (Fig. 2G). CD detection showed that PD-HAP1 had a positive peak at 209 nm and PL-HAP1 had a negative peak at 209 nm under low concentration of PTAR (Fig. 2H). PD-HAP2 had a positive peak at 236 nm, and PL-HAP2 had a negative peak at 237 nm under high concentration of PTAR (Fig. 2I). These results demonstrated that the chirality of PTAR changes the interaction between HAP molecules, causing molecular rearrangement and inducing a significant CD signal.

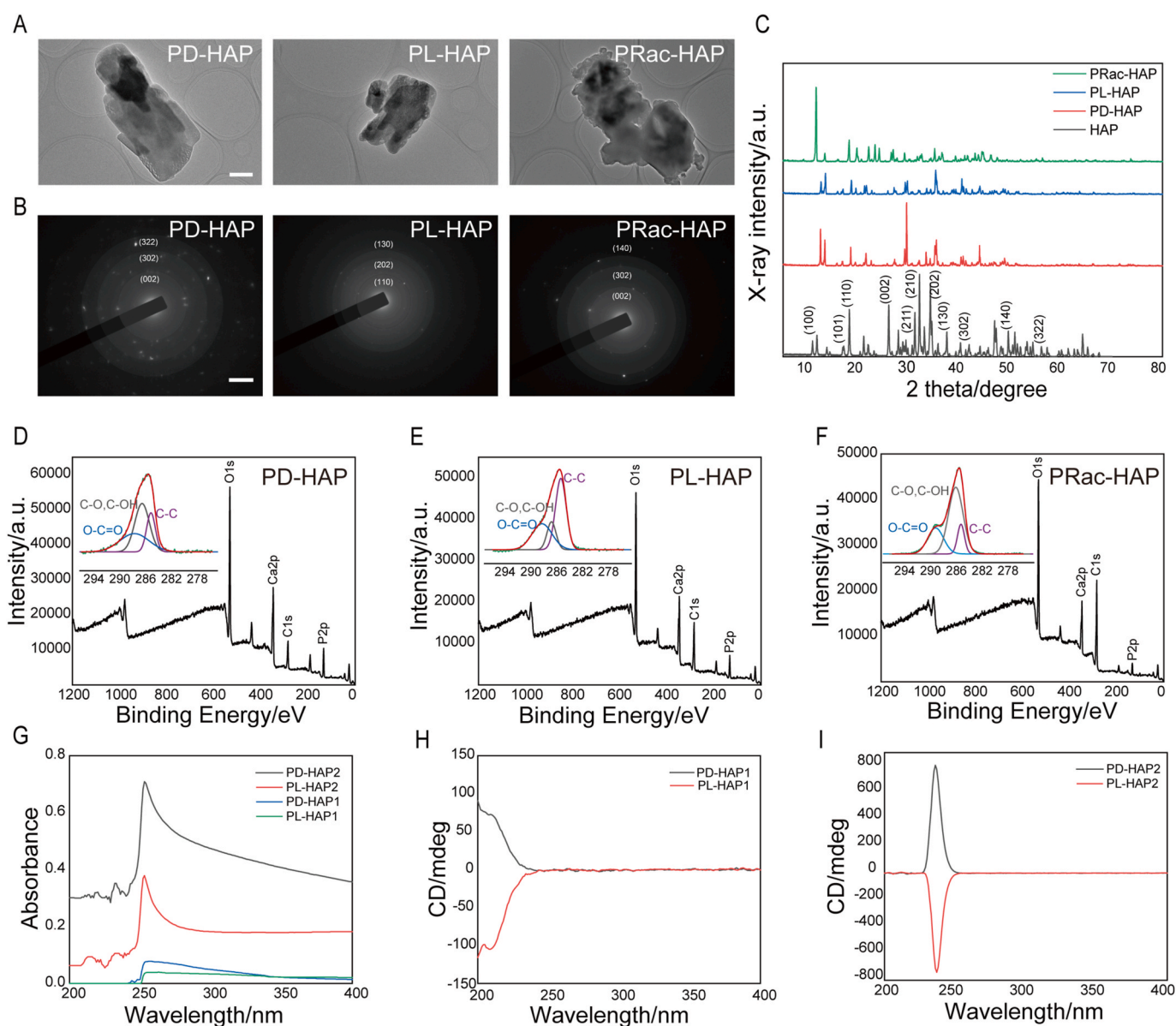


Fig. 2. The characteristics of the chiral HAPs. (A) TEM images of PD-HAP, PL-HAP and PRac-HAP. Scale bars: 500 nm. (B) SAED images of PD-HAP, PL-HAP and PRac-HAP. Scale bars: 2 nm^{-1} . (C) XRD images of PD-HAP, PL-HAP and PRac-HAP. (D–F) XPS survey spectra recorded for (D) PD-HAP, (E) PL-HAP, and (F) PRac-HAP powders. Insert figures are C 1s high-resolution spectra of (D) PD-HAP, (E) PL-HAP, and (F) PRac-HAP powders. (G) UV–vis spectra of PD-HAP1, PL-HAP1, PD-HAP2, and PL-HAP2 powders. (H) CD spectra of PD-HAP1 and PL-HAP1 powders. (I) CD spectra of PD-HAP2 and PL-HAP2 powders.

3.2. PL-HAP changed shape and promoted migration

To verify the biocompatibility of chiral HAPs, MC3T3-E1 cells were co-cultured with chiral HAPs of different configurations (Fig. 3A). According to previous studies, the cell viabilities were estimated by incubating with different concentrations of chiral HAPs ranging from 50 to 400 $\mu\text{g}/\text{mL}$ [24]. After three days of culture, the CCK-8 detection showed that the cell viabilities of MC3T3-E1 cells cultured with four concentrations of HAPs with different configurations were more than 70 % (Fig. 2B). After the MC3T3-E1 cells were induced osteogenic differentiation, the contact between cells was closer, and the cell fibrous shape was more obvious and had certain directivity, forming a calcified bone-like structure [25]. Cell morphology changed when MC3T3-E1 cells differentiated into osteoblasts, so cytoskeletal F-actin stainings were performed on different groups of cells (Fig. 2C, Fig. S3). The effect of PL-HAP on cell morphology was particularly obvious, while that of PD-HAP and PRac-HAP was no difference. Cell live/dead staining showed that there were few dead cells in different chiral HAPs groups (Fig. 2D, E, Fig. S4), which proved that the chiral HAPs had no cytotoxicity and good biocompatibility. The loss of cells affected the process of bone healing in the bone injury area, thus it was particularly important to guide the migration of cells to the defect site. It has been reported that chirality can guide cell migration, and the materials with different configurations had different migration effects on cells [26]. To investigate the effect of HAPs with different configurations on MC3T3-E1 cells migration, Transwell migration (Fig. 3F, G, I, Fig. S5) and scratch wound-healing assay (Fig. 3H, J, Fig. S6) assay were performed. The mobility of PL-HAP-treated cells was the highest in the polymer-treated group. In addition, the migration of MC3T3-E1 cells to the medium containing HAPs in Transwell cells also verified that the mobility of PL-HAP groups was the highest. It was proved that HAPs with a left-handed configuration can promote the migration of pre-osteoblasts, and HAPs with a right-handed or racemic configuration did not affect cell migration.

3.3. PL-HAP promoted migration and angiogenesis

The process of bone repair required a lot of nutrients, so angiogenesis and the extension of blood vessels to the bone repair area were particularly important. To confirm the effect of chiral HAPs on angiogenesis, different configurations of HAPs were used to treat endothelial cells to promote angiogenesis. The cell viabilities of HUVEC cells were all over 70 % after co-culture with HAPs of different concentrations (400, 200, 100, 50 $\mu\text{g}/\text{mL}$) and different configurations (Fig. 4A, Fig. S7). Cell live/dead staining also showed almost no dead cells (Fig. 4B, Figs. S8 and S9), which demonstrated in vitro chiral HAPs were not cytotoxic to HUVEC cells. Moreover, various concentrations of chiral HAPs were not cytotoxic to L929 cells by the CCK-8 assay and the live/dead staining (Figs. S13A–D). In general, the results verified that the chiral HAPs showed excellent biocompatibility to different types of cells, and its biocompatibility was universal. To investigate the universality of cellular migration promoted by chiral HAPs, scratch wound-healing assay, and Transwell migration assay were performed on HUVEC cells and L929 cells, respectively. The cell migration ability of HUVEC cells treated with PL-HAP was best in the polymer-induced HAP groups (Fig. 4C–F, Figure S10, S11). For the wound-healing assay of L929 cells, the migration of L929 cells ability in PL-HAP group was significantly promoted than those in PRac-HAP group and the control group (Figs. S13E–H). It was demonstrated that PLTA-induced HAP also promoted fibroblast migration. Hence, this effect of promoting migration was proved to be universal in cells.

Monomolecule-induced chiral substances had been proven to have a role in vascular remodeling including promoting angiogenesis and rebuilding the blood transport system, but the effect of polymer-induced chirality on angiogenesis had not been explored. The tube formation experiment showed that the number of branch points in the PL-HAP

group was significantly more than that in the PD-HAP group. Meanwhile, there was a trend to significance ($p = 0.0660$) between the PL-HAP group and the PRac-HAP group (Fig. 4G and H). In addition, the expression of VEGFA, a gene related to angiogenesis, was higher than that of PD-HAP and PRac-HAP-treated HUVEC cells (Fig. 4I, Fig. S12). In a word, the number of branch points in PLTA-induced groups exhibited a difference, the great ability of PL-HAP to induce endothelial cells to migrate and generate branch points proved the difference between chiral polymer inducers in angiogenesis.

3.4. PL-HAP induced osteogenic differentiation

Chirality had the ability to regulate not only stem cell differentiation, but also osteogenic differentiation of osteogenic precursor cells [27]. We studied the in vitro responses of pre-osteoblasts MC3T3-E1 cells in order to directly verify the osteogenic effect of different chiral HAPs configurations. ALP staining and ARS staining of MC3T3-E1 cells had been developed as the basic method for analyzing osteogenic differentiation. In specific, the cells were seeded in the 24-well plates were co-cultured with chiral HAPs, and then stained with ALP marker and ARS at pre-determined time points, respectively. ALP staining showed a significant difference at 7 days, and the staining area of cells in the PL-HAP group was larger than other groups, indicating that the effects of osteogenic differentiation was outstanding in the group (Fig. 5A and B). The results of ARS staining were in accordance with the above results at 14 days (Fig. 5C and D). At 14 days and 21 days, ALP and ARS staining and quantitative results showed that the effects of osteogenic differentiation were significantly promoted in the PL-HAP group, proving the potential abilities of the polymer chiral inducer (Fig. S14). MC3T3-E1 cells can be induced to express ALP protein, runt-related transcription factor 2 (Runx2), and bone gamma-carboxyglutamate (gla) protein (Bglap) under osteogenic differentiation conditions, and the increased expression of these proteins proved the ability of HAP to induce osteogenic differentiation of cells [28]. To further study the effect of promoting osteogenesis, the differential expressions of osteogenic-related proteins were determined by immunofluorescence. The expressions of ALP and Runx2 protein in the PL-HAP group were significantly higher than those in the other groups on day 8, revealing that PL-HAP promoted the protein expression of osteoblasts (Fig. 5E–H, Fig. S15). And the Bglap protein expression of the PL-HAP-treated group was significantly increased in the polymer-induced HAP group at 3 days (Fig. S16).

Furthermore, the effects of HAP configurations on mRNA expression levels were investigated by the RT-qPCR, selecting Sp7, COL1a1, BMP-2, and Runx2 as osteogenic markers. After co-culture of MC3T3-E1 cells with different chiral HAPs, the mRNA expression of cells was detected (Fig. 5I–L). The expression of Sp7, COL1a1, BMP-2, and Runx2 in MC3T3-E1 cells treated with PL-HAP all started to show a significant rise, while the expressions of the osteogenic markers in PD-HAP and PRac-HAP treated cells were lower. And high concentration of PL-HAP could also effectively promote osteogenic differentiation (Fig. S17). Chiral HAPs released Ca^{2+} in the process of interpretation, resulting in increased extracellular Ca^{2+} concentration, affecting osteogenic differentiation of MC3T3-E1 cells, resulting in increased intracellular Ca^{2+} levels. In this way, Ca^{2+} entered the cell through the calcium channel, activated ERK/MAPK signaling pathway, and then affected the expression of BMP-2 [29]. Jun was a transcription factor regulated by ERK/MAPK signaling pathway, and the expression of its gene reflected whether the ERK/MAPK signaling pathway was activated. As shown in Fig. 5M, the expression of Jun gene in the PL-HAP group was significantly higher than that in the other two groups, which directly reflected that PL-HAP effectively activated the ERK/MAPK signaling pathway and promoted the development of cells towards osteoblasts. At the same time, Ca^{2+} could promote the expression of cAMP signaling pathway and further induce the increase of MAPK [30]. As a key enzyme of cAMP signaling pathway, the high expression of AC gene implied the activation of cAMP signaling pathway. The expression of AC gene in the

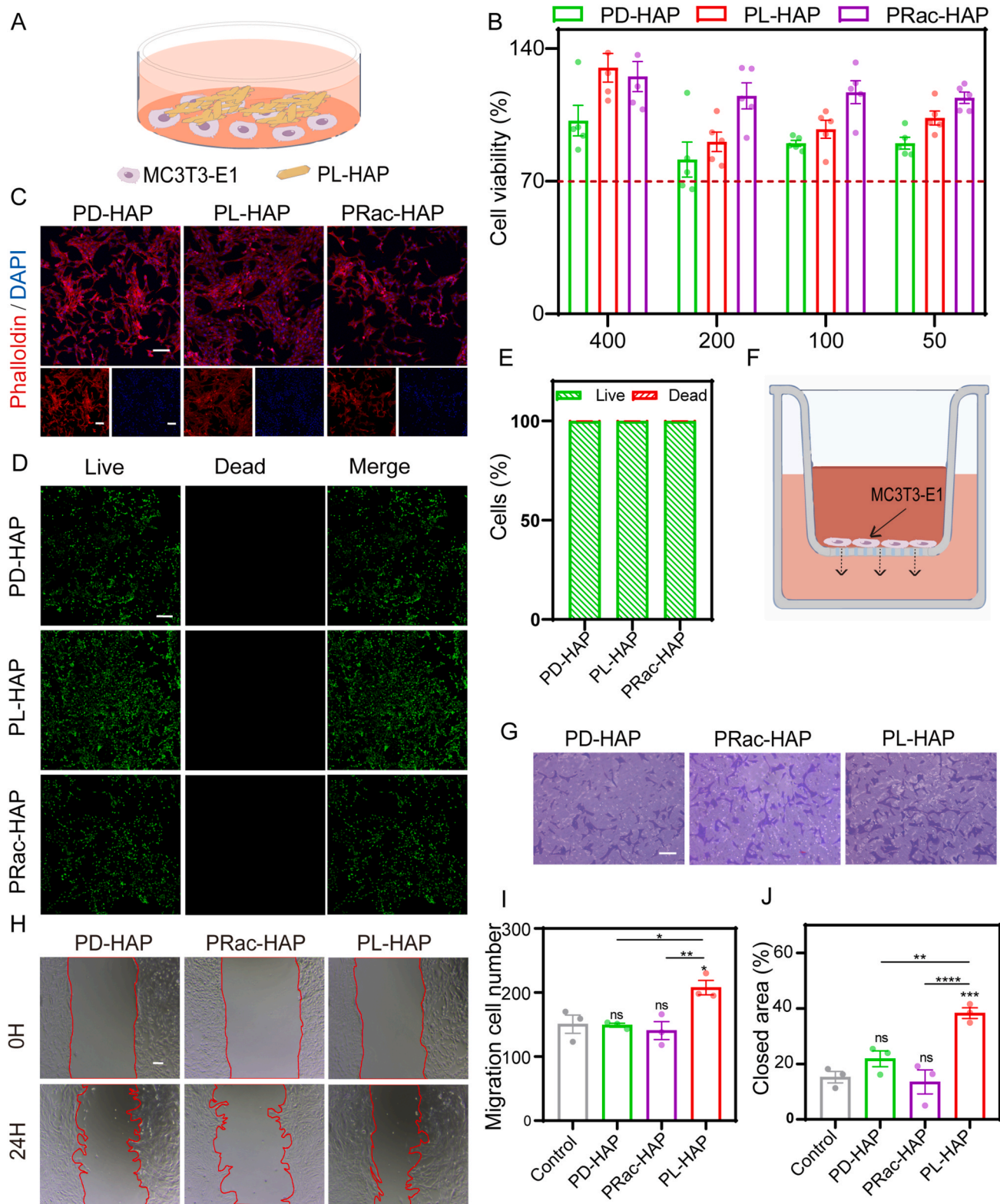


Fig. 3. Biocompatibility of the chiral HAPs and ability to migrate of MC3T3-E1 cells. (A) Diagram of co-culture of PL-HAP and MC3T3-E1 cells. (B) Cell viability of MC3T3-E1 cells cultured with the chiral HAPs examined by CCK-8 assay. Error bars: standard error (n = 5). (C) F-actin fluorescence staining images of MC3T3-E1 cells cultured with the chiral HAPs. Scale bars: 100 μm. (D) Cell live/dead staining images of MC3T3-E1 cells cultured with the chiral HAPs. Scale bars: 100 μm. (E) Semi-quantitative diagram of cell live/dead staining. (F) Schematic diagram of MC3T3-E1 cells migration in the Transwell small room. (G) Diagrams of the migration results of MC3T3-E1 cells treated with chiral HAPs. Scale bars: 100 μm. (H) Diagrams of the scratch healing results of MC3T3-E1 cells treated with chiral HAPs. Scale bars: 100 μm. (I) Quantitative analysis of the migration experiment. **p* < 0.05, ***p* < 0.01, ns: no difference. Error bars: standard error (n = 3). (J) Quantitative analysis of the scratch healing experiment. ***p* < 0.01, ****p* < 0.001, and *****p* < 0.0001, ns: no difference. Error bars: standard error (n = 3).

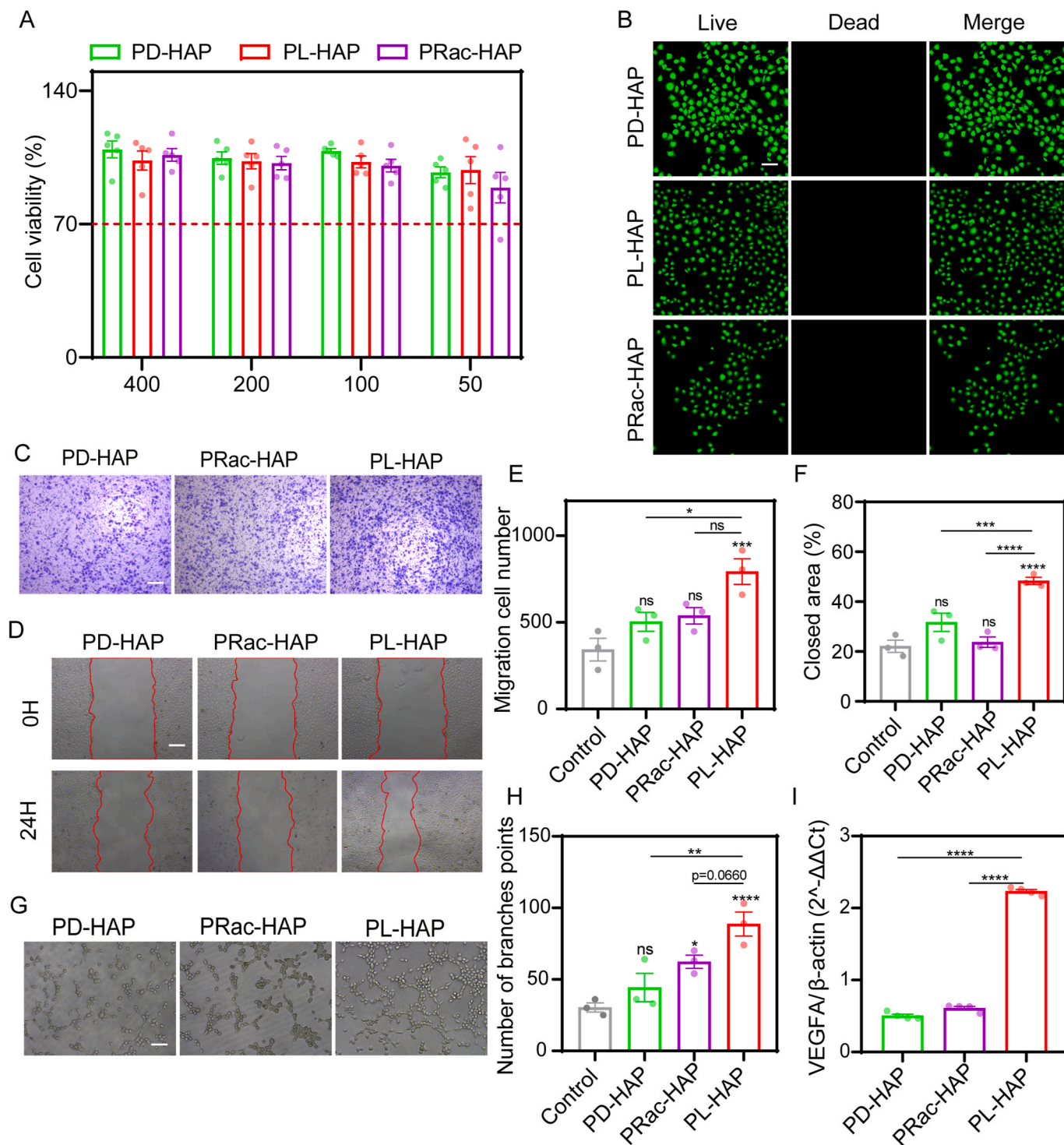


Fig. 4. Biological effects of chiral HAPs on HUVEC cells. (A) Cell viability of HUVEC cells cultured with the chiral HAPs examined by CCK-8 assay. Error bars: standard error (n = 5). (B) Cell live/dead staining images of HUVEC cells cultured with the chiral HAPs. Scale bars: 100 μ m. (C) Diagram of the migration results of HUVEC cells treated with chiral HAPs. Scale bars: 200 μ m. (D) Diagram of the scratch healing results of HUVEC cells treated with chiral HAPs. Scale bars: 100 μ m. (E) Quantitative analysis of the migration experiment. * $p < 0.05$, *** $p < 0.001$, ns: no difference. Error bars: standard error (n = 3). (F) Quantitative analysis of the scratch healing experiment. *** $p < 0.001$, **** $p < 0.0001$, ns: no difference. Error bars: standard error (n = 3). (G) Diagram of the tubule formation assay of HUVEC cells treated with chiral HAPs. Scale bars: 50 μ m. (H) Quantitative analysis of the tubule formation assay. * $p < 0.05$, ** $p < 0.01$, **** $p < 0.0001$, ns: no difference. Error bars: standard error (n = 3). (I) Expression level of angiogenic gene VEGFA. **** $p < 0.0001$. Error bars: standard error (n = 4).

PL-HAP group was significantly better than that in the other two groups (Fig. 5N), which also proved that PL-HAP activated the cAMP signaling pathway.

4. Conclusion

Generally speaking, PTAR was a dihydroxy-carboxylic acid polymer that could be used as an inducer in chiral transfer systems. The chiral polymer inducer, PLTA, could easily induce the PL-HAP chiral

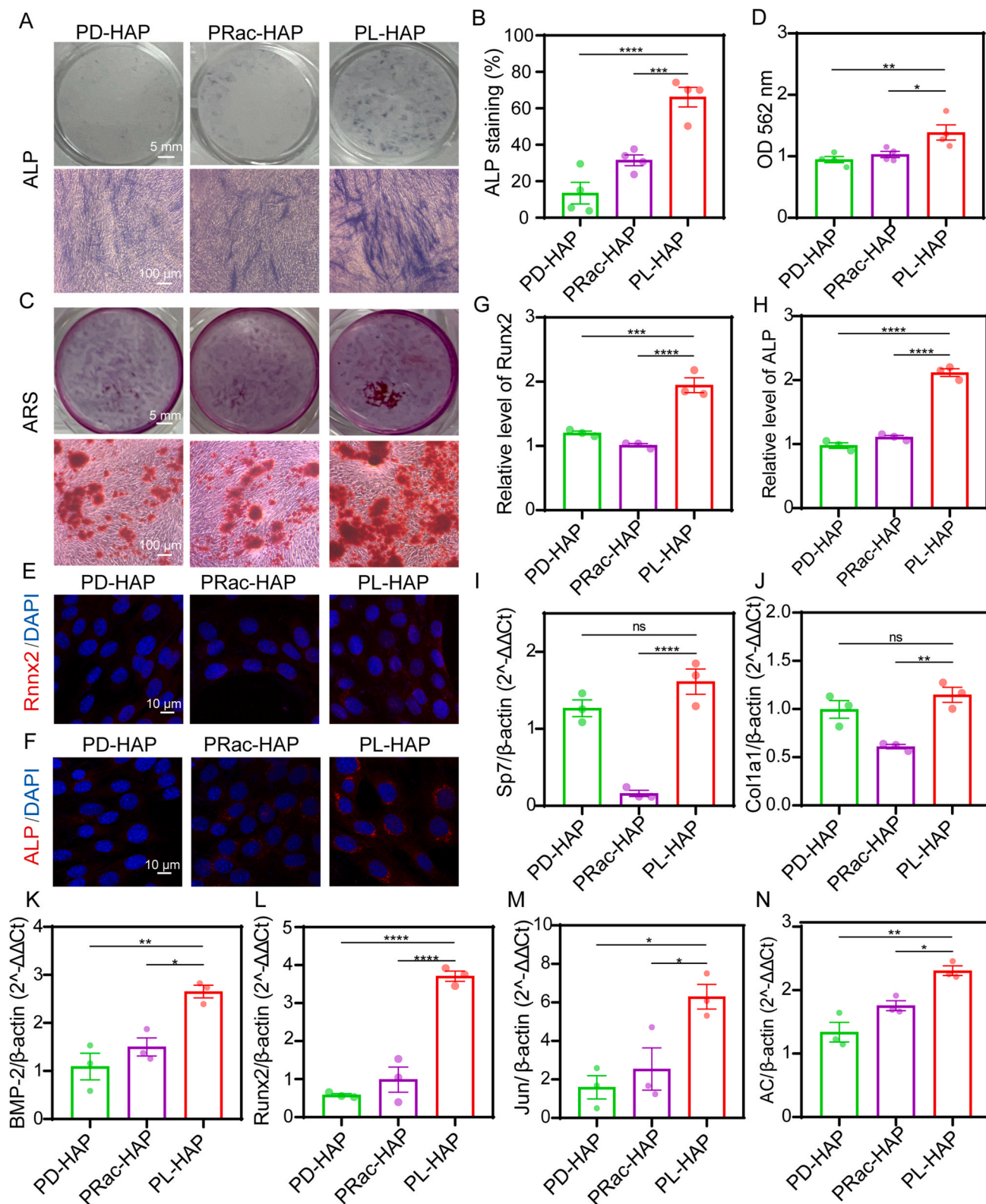


Fig. 5. Effect of chiral HAPs on osteogenic differentiation ability of preosteoblasts. (A) ALP staining plots of co-culture of chiral HAPs with MC3T3-E1 cells after 7 days. (B) Quantitative analysis of ALP staining. *** $p < 0.001$, **** $p < 0.0001$. Error bars: standard error (n = 4). (C) ARS staining plots of co-culture of chiral HAPs with MC3T3-E1 cells after 14 days. (D) Quantitative analysis of ARS staining. * $p < 0.05$, ** $p < 0.01$. Error bars: standard error (n = 4). (E, F) Runx2 and ALP protein expression of MC3T3-E1 with chiral HAPs. (G, H) Semi-quantitative analyses of Runx2 and ALP protein staining. *** $p < 0.001$, **** $p < 0.0001$. Error bars: standard error (n = 3). (I–M) Sp7, Col1a1, BMP-2, and Runx2 mRNA expression of co-culture of MC3T3-E1 cells with chiral HAPs. * $p < 0.05$, ** $p < 0.01$, **** $p < 0.0001$, ns: no difference. Error bars: standard error (n = 3). (M, N) Jun and AC mRNA expression of co-culture of MC3T3-E1 cells with chiral HAPs. * $p < 0.05$, ** $p < 0.01$. Error bars: standard error (n = 3).

configuration, which was more likely to promote cell migration. The results of this study showed that PL-HAP could promote the angiogenesis of endothelial cells and osteogenic differentiation of pre-osteoblasts. It indicated that PL-HAP provided a good microenvironment for bone defect sites by promoting angiogenesis to promote osteogenesis. This study preliminarily explored the possible mechanism of HAP osteogenesis induced by chiral polymer inducers, PL-HAP declined into Ca^{2+} and PO_4^{3-} in the cellular microenvironment, and Ca^{2+} could enter cells through calcium channels and affect the ERK/MAPK and cAMP signaling pathways, resulting in increased expression of genes related to bone regeneration.

CRedit authorship contribution statement

Zongying Zhang: Writing – original draft, Software, Methodology, Investigation, Data curation. **Bing Liang:** Software, Methodology, Data curation. **Dan Wang:** Software, Methodology, Investigation. **Ying Zhang:** Software, Methodology, Investigation. **Zhongmin Geng:** Writing – review & editing, Writing – original draft, Visualization, Validation, Supervision, Software, Resources, Project administration, Methodology, Investigation, Funding acquisition, Formal analysis, Data curation, Conceptualization. **Dongming Xing:** Writing – review & editing, Writing – original draft, Visualization, Validation, Supervision, Software, Resources, Project administration, Methodology, Investigation, Funding acquisition, Formal analysis, Data curation, Conceptualization.

Declaration of competing interest

The authors declare that they have no known competing financial interests or personal relationships that could have appeared to influence the work reported in this paper.

Acknowledgement

Z.Z. and B.L. contributed equally to this work. This work was financially supported by the National Natural Science Foundation of China (22275105). The Young Experts of Taishan Scholar Project under Grant tsqn 202306177.

Appendix A. Supplementary data

Supplementary data to this article can be found online at <https://doi.org/10.1016/j.mtbio.2025.101460>.

Data availability

Data will be made available on request.

References

- [1] Y.Y. Duan, S.A. Che, Chiral mesostructured inorganic materials with optical chiral response, *Adv. Mater.* 35 (2023) 28.
- [2] M. Inaki, J.Y. Liu, K. Matsuno, Cell chirality: its origin and roles in left-right asymmetric development, *Philos. Trans. R. Soc. B-Biol. Sci.* 371 (2016) 9.
- [3] E.D. Scheeff, J.L. Fink, Fundamentals of protein structure, *Methods Biochem. Anal.* 44 (2003) 15–39.
- [4] J.D. Watson, F.H.C. Crick, Molecular structure of nucleic acids - a structure for deoxyribose nucleic acid, *Am. J. Psychiatr.* 160 (2003) 623–624.
- [5] P. Fratzl, Biomimetic materials research: what can we really learn from nature's structural materials? *J. R. Soc. Interface* 4 (2007) 637–642.
- [6] C.H. Turner, D.B. Burr, Basic biomechanical measurements of bone - a tutorial, *Bone* 14 (1993) 595–608.
- [7] C. Zhou, A.Q. Liu, P. Li, J. Ai, L. Han, S.Y. Zhang, S. Chen, Y.M. Ouyang, B.J. Li, S. A. Che, C.Y. Fan, Chiral mesostructured hydroxyapatite on 3D macroporous coralline scaffolds for enantio-selective osteogenesis, *Mater. Adv.* 4 (2023) 5817–5826.
- [8] G.L. Koons, M. Diba, A.G. Mikos, Materials design for bone-tissue engineering, *Nat. Rev. Mater.* 5 (2020) 584–603.
- [9] S. Weiner, H.D. Wagner, The material bone: structure mechanical function relations, *Annu. Rev. Mater. Sci.* 28 (1998) 271–298.
- [10] J. Zhou, Z. Zhang, J. Joseph, X. Zhang, B.E. Ferdows, D.N. Patel, W. Chen, G. Banfi, R. Molinaro, D. Cosco, N. Kong, N. Joshi, O.C. Farokhzad, C. Corbo, W. Tao, Biomaterials and nanomedicine for bone regeneration: progress and future prospects, *Exploration* 1 (2021) 12.
- [11] C.J. Shuai, B. Peng, P. Feng, L. Yu, R.L. Lai, A.J. Min, In situ synthesis of hydroxyapatite nanorods on graphene oxide nanosheets and their reinforcement in biopolymer scaffold, *J. Adv. Res.* 35 (2022) 13–24.
- [12] H. Moussa, W.G. Jiang, A. Alshegri, A. Mansour, A. El Hadad, H.H. Pan, R. K. Tang, J. Song, J. Vargas, M.D. McKee, F. Tamimi, High strength brushite bioceramics obtained by selective regulation of crystal growth with chiral biomolecules, *Acta Biomater.* 106 (2020) 351–359.
- [13] N. Reznikov, M. Bilton, L. Lari, M.M. Stevens, R. Kroger, Fractal-like hierarchical organization of bone begins at the nanoscale, *Science* 360 (2018) 507–516.
- [14] B. Alexander, T.L. Daulton, G.M. Genin, J. Lipner, J.D. Pasteris, B. Wopenka, S. Thomopoulos, The nanometre-scale physiology of bone: steric modelling and scanning transmission electron microscopy of collagen-mineral structure, *J. R. Soc. Interface* 9 (2012) 1774–1786.
- [15] M.M. Giraud-Guille, Twisted plywood architecture of collagen fibrils in human compact bone osteons, *Calcif. Tissue Int.* 42 (1988) 167–180.
- [16] C. Zhou, S.Y. Zhang, J. Ai, P. Li, Y.J. Zhao, B.J. Li, L. Han, Y.Y. Duan, S.N. Che, Enantioselective interaction between cells and chiral hydroxyapatite films, *Chem. Mater.* 34 (2022) 53–62.
- [17] Z.C. Cai, C. Qu, W. Song, H.Y. Wang, S. Chen, C. Zhou, C.Y. Fan, Hierarchical chiral calcium silicate hydrate films promote vascularization for tendon-to-bone healing, *Adv. Mater.* (2024) 16.
- [18] T.F. Miao, X.X. Cheng, Y.Q. Guo, G. Zhang, W. Zhang, Preparation of chiral polymers: precise chirality transfer from natural species to achiral artificial polymers, *Giant* 14 (2023) 18.
- [19] G.A. Hembury, V.V. Borovkov, Y. Inoue, Chirality-sensing supramolecular systems, *Chem. Rev.* 108 (2008) 1–73.
- [20] C.J. Shuai, X.X. Shi, K. Wang, Y.L. Gu, F. Yang, P. Feng, Ag-doped CNT/HAP nanohybrids in a PLLA bone scaffold show significant antibacterial activity, *Bio-Des. Manuf.* 7 (2024) 105–120.
- [21] A.M. Jalaludeen, R. Ramakrishnan, S.S. Gunasekaran, N. Thajuddin, M.K. Selvam, B.M.S. Ali, R. Dua, P. Ramakrishnan, M.D. Ramesh, S. Vinayagam, R. Rajamohan, T. Sundaram, Advancements in hydroxyapatite synthesis and surface modifications for emerging biomedical applications, *Inorg. Chem. Commun.* 170 (2024) 19.
- [22] A. Nan, X. Filip, M. Dan, O. Marincas, Clean production of new functional coatings of magnetic nanoparticles from sustainable resources, *J. Clean. Prod.* 210 (2019) 687–696.
- [23] H.J. Wang, H.Y. Zhang, H.Y. Zhang, G.X. Liu, X.Y. Dai, H. Wu, Y. Liu, Guest-induced supramolecular chirality transfer in 2 pseudorotaxanes: experimental and computational study, *Org. Biomol. Chem.* 18 (2020) 7649–7655.
- [24] W. Xu, C. Xu, J.L. Yi, H.L. Dai, The effect of different hydroxyapatite microparticles on the osteogenic differentiation of MC3T3-E1 preosteoblasts, *J. Mat. Chem. B* 6 (2018) 5234–5242.
- [25] A.K. Yip, A.T. Nguyen, M. Rizwan, S.T. Wong, K.H. Chiam, E.K.F. Yim, Anisotropic traction stresses and focal adhesion polarization mediates topography-induced cell elongation, *Biomaterials* 181 (2018) 103–112.
- [26] P.F. Duan, H. Cao, L. Zhang, M.H. Liu, Gelation induced supramolecular chirality: chirality transfer, amplification and application, *Soft Matter* 10 (2014) 5428–5448.
- [27] X. Yao, Y.W. Hu, B. Cao, R. Peng, J.D. Ding, Effects of surface molecular chirality on adhesion and differentiation of stem cells, *Biomaterials* 34 (2013) 9001–9009.
- [28] Q. Zeng, H.M. Zheng, B.C. Heng, W.T. Yao, Y. Yang, S.J. Jiang, X.L. Deng, Chirality-biased protein expression profile during early stages of bone regeneration, *Front. Bioeng. Biotechnol.* 11 (2023) 11.
- [29] A.M.C. Barradas, H.A.M. Fernandes, N. Groen, Y.C. Chai, J. Schrooten, J. van de Peppel, J. van Leeuwen, C.A. van Blitterswijk, J. de Boer, A calcium-induced signaling cascade leading to osteogenic differentiation of human bone marrow-derived mesenchymal stromal cells, *Biomaterials* 33 (2012) 3205–3215.
- [30] D. Xu, Y.X. Wan, Z.H. Li, C.B. Wang, Q.X. Zou, C. Du, Y.J. Wang, Tailorable hierarchical structures of biomimetic hydroxyapatite micro/nano particles promoting endocytosis and osteogenic differentiation of stem cells, *Biomater. Sci.* 8 (2020) 3286–3300.